

Supporting information

Chemomechanical coupling in hexameric protein-protein interfaces harness energy within V-type ATPases

Abhishek Singharoy,[†] Christophe Chipot,^{*,‡,†,¶} Mahmoud Moradi,[§] and
Klaus Schulten^{†,¶}

Theoretical and Computational Biophysics Group, Beckman Institute for Advanced Science and Technology, University of Illinois at Urbana-Champaign, 405 North Mathews Avenue, Urbana, Illinois 61801, Laboratoire International Associé Centre National de la Recherche Scientifique et University of Illinois at Urbana-Champaign, Unité Mixte de Recherche n°7565, Université de Lorraine, B.P. 70239, 54506 Vandœuvre-lès-Nancy cedex, France, Department of Physics, University of Illinois at Urbana-Champaign, 1110 West Green Street, Urbana, Illinois 61801, and Biomolecular Simulations Group, Department of Chemistry and Biochemistry, University of Arkansas, Fayetteville, Arkansas 72701

E-mail: chipot@ks.uiuc.edu

*To whom correspondence should be addressed

[†]Theoretical and Computational Biophysics Group, Beckman Institute for Advanced Science and Technology, University of Illinois at Urbana-Champaign, 405 North Mathews Avenue, Urbana, Illinois 61801

[‡]Laboratoire International Associé CNRS/UIUC

[¶]Department of Physics, University of Illinois at Urbana-Champaign, 1110 West Green Street, Urbana, Illinois 61801

[§]University of Arkansas

Methods

Table S1: Summary of the different simulations performed to decrypt the chemomechanical coupling in V_1 -rotor.

Method	Simulation time (μs)				
	TMD ^a	SMWST ^b	BEUS ^c	MCMD ^d	FEP ^e
A_3B_3	0.3	20.0	—	—	1.32 ^f
A_3B_3 -DF	0.3	8.0	28.0 ^g	7.0	—
Total			64.92		

^a targeted molecular dynamics, ¹ ^b string method with swarms of trajectories, ² ^c biased-exchange umbrella sampling, ³ ^d multiple-copy molecular dynamics without exchange, ^e free-energy perturbation. ^{4,5} ^f 0.264 μs for each of the five configurations ATP (**t**), ATP (**b**), ATP (**e**), ADP+P_i (**t**) and ADP+P_i (**e**) — see Table S2 for additional detail, ^g 14 μs for each of the two configurations for ADP+P_i (**b**) and ADP+P_i (**b**), decomposed in 175 images \times 20 replicas per image \times 4 ns per replica.

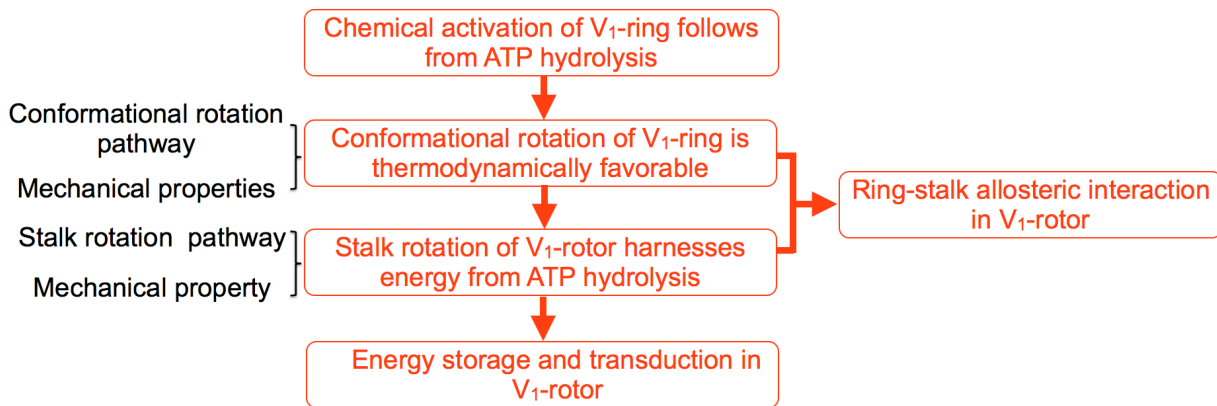


Figure S1: Flowchart of the section titles, summarizing key findings of the computational investigation, to facilitate navigation through the Results section.

Table S2: Summary of the standard binding free-energy calculations performed for ATP and ADP + P_i bound to the catalytic domain of V₁-rotor.

Contribution	Simulation time (ns)	Free-energy change (kcal/mol)
ATP, tightly bound (t)		
$\Delta G_{\text{alch}}^{\text{bound, a}}$	125	-443.5 ± 0.4
$\Delta G_{\text{restr}}^{\text{bound, b}}$	7	14.8 ± 0.3
$\Delta G_{\text{restr}}^{\text{free, c}}$	7	-16.1 ± 0.1
$\Delta G_{\text{alch}}^{\text{free, d}}$	125	433.2 ± 0.6
$\Delta G_{\text{bind}}^{\text{o, e}}$		-11.6 ± 0.8
ATP, bound (b)		
$\Delta G_{\text{alch}}^{\text{bound}}$	125	-441.8 ± 0.8
$\Delta G_{\text{restr}}^{\text{bound}}$	7	16.5 ± 0.5
$\Delta G_{\text{restr}}^{\text{free}}$	7	-16.3 ± 0.1
$\Delta G_{\text{alch}}^{\text{free}}$	125	433.2 ± 0.6
$\Delta G_{\text{bind}}^{\text{o}}$		-8.9 ± 1.1
ATP, empty (e)		
$\Delta G_{\text{alch}}^{\text{bound}}$	125	-438.4 ± 0.8
$\Delta G_{\text{restr}}^{\text{bound}}$	7	17.4 ± 0.6
$\Delta G_{\text{restr}}^{\text{free}}$	7	-16.3 ± 0.1
$\Delta G_{\text{alch}}^{\text{free}}$	125	433.2 ± 0.6
$\Delta G_{\text{bind}}^{\text{o}}$		-4.1 ± 1.1
ADP + P_i, tightly bound (t)		
$\Delta G_{\text{alch}}^{\text{bound}}$	125	-442.0 ± 0.4
$\Delta G_{\text{restr}}^{\text{bound}}$	7	15.9 ± 0.5
$\Delta G_{\text{restr}}^{\text{free}}$	7	-18.4 ± 0.1
$\Delta G_{\text{alch}}^{\text{free}}$	125	436.2 ± 0.6
$\Delta G_{\text{bind}}^{\text{o}}$		-8.3 ± 0.9
ADP + P_i, empty (e)		
$\Delta G_{\text{alch}}^{\text{bound}}$	125	-439.3 ± 0.1
$\Delta G_{\text{restr}}^{\text{bound}}$	7	17.2 ± 0.5
$\Delta G_{\text{restr}}^{\text{free}}$	7	-18.4 ± 0.1
$\Delta G_{\text{alch}}^{\text{free}}$	125	436.2 ± 0.6
$\Delta G_{\text{bind}}^{\text{o}}$		-4.3 ± 0.8

^a alchemical free-energy change in the bound state, ^b free-energy change due to the conformational, positional and orientational restraints imposed in the bound state, ^c free-energy change due to the conformational restraint imposed in the free state and the analytical terms for the translation and rotation of a rigid substrate in a homogenous liquid, ^d alchemical free-energy change in the free state, ^e standard binding free energy.

Alchemical calculations. Computational details

To avoid singularities in the van der Waals potential, which arise in alchemical transformations when atoms of the substrate, either ATP or ADP+P_i, appear at a location in space already occupied by other particles, use was made of a separation-shifted scaling soft-core potential⁶ with a scaling factor of 4.0. Electrostatic decoupling was applied as the substrate was removed from, or introduced in its environment, turning electrostatic interactions on or off twice as fast as van der Waals interactions. To prevent the substrate from drifting away from the catalytic domain of V₁-rotor, we tethered it by means of geometric restraints acting on collective variables to the conformation, position and orientation in the native state (see Figure S2). Towards this end, groups of atoms pertaining to the enzyme and to the nucleotide were selected, allowing unambiguous definition of the latter with respect to the former through the introduction of the relevant polar coordinates and Euler angles. In addition, the conformation of the substrate was frozen by imposing that the distance root mean-square deviation (RMSD) with respect to that of the native state be equal to zero. The free-energy contributions arising from the loss of configurational entropy due to these geometric restraints were estimated in independent thermodynamic-integration simulations, wherein the force constant of the harmonic potentials at play was turned reversibly to zero. In the bound states — either tightly bound (t), bound (b) or empty (e), all contributions can be determined in a single free-energy calculation, from whence the different gradients can be extracted and subsequently integrated. For the three bound states and for each substrate, turning the force constant from its nominal value to zero was stratified in 500 λ -points, at which the integrand was computed over 25 ps of data collection, following 100 ps of thermalization. A separate simulation was performed in the bulk state to evaluate the conformational term, while the other contributions characterizing the translation and the rotation of a rigid body in an isotropic environment are determined analytically.⁷ The simulation consisted of 500 λ -points, at which 25 ps of thermalization prefaced 100 ps of data collection.

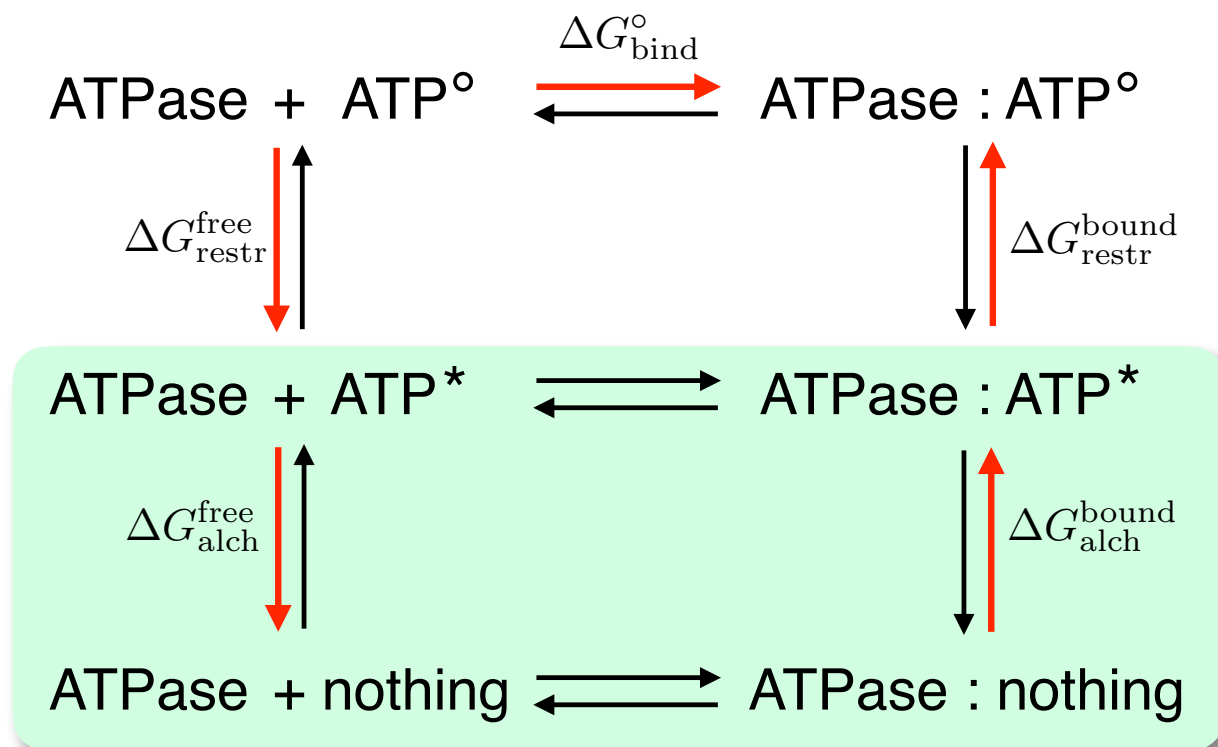


Figure S2: Thermodynamic cycle utilized to determine the standard binding free energy of ATP to the catalytic domain of V_1 -rotor. The alchemical free-energy calculation in the bound ($\Delta G_{\text{bound}}^{\text{alch}}$) and in the unbound ($\Delta G_{\text{free}}^{\text{alch}}$) states, highlighted in the green box, is carried out on the nucleotide (ATP^*) restrained to its native conformation, position and orientation in the bound complex by means of suitably chosen harmonic potentials.⁷ The free-energy contribution that corresponds to the loss of configurational entropy arising from the geometrical restraints, i.e., the difference between the restrained (ATP^*) and the free (ATP°) substrate, is evaluated in separate simulations, both in the bound ($\Delta G_{\text{bound}}^{\text{restr}}$) and in the ($\Delta G_{\text{free}}^{\text{restr}}$) states.

Estimating the error associated to a computed free-energy change constitutes a difficult, often overlooked task, which can be explained in large measure by the convoluted nature of the sources of error responsible for the discrepancy between theoretical and experimental measures. From a dogmatic perspective, failure to provide convincing error bars is also rooted in the common belief that a single simulation cannot provide both a free-energy difference and the error associated to it with an equal accuracy. From the standpoint of numerical simulations, the error associated to a free-energy change has a systematic origin, which primarily stems from finite sampling, and a statistical origin related to the width of the underlying probability distributions.⁸ In a more general sense, systematic errors also embrace force-field inaccuracies, as well as algorithmic artifacts, albeit these contributions are evidently more cumbersome to appreciate. Ideally, any free-energy

change ought to be estimated from a series of independent simulations, assumed to sample distinct regions of phase space. Given the complexity of the alchemical transformations examined here and the length of the free-energy calculations to warrant convergence (see Table 2), repeating the latter would obviously be intractable. We resort to provide as a measure of the error associated to the different contributions to the binding affinity the hysteresis between the forward and the backward transformation, and apply the Bienayme formula, assuming that each contribution corresponds to an independent observable.

Theoretical framework for the free–energy estimation along the minimum free–energy path

Suppose that the dynamics of a high-dimensional atomic system $\{\mathbf{x}\}$ can be simplified as an effective dynamics in a coarse variable space ζ . The effective dynamics can be described by a Brownian motion in the ζ space with an effective potential energy $G(\zeta)$ and diffusion tensor $\mathbf{D}(\zeta)$. The former is the potential of mean force (PMF) of the atomic system in the ζ space and the latter is generally position-dependent and anisotropic.⁹ One may sample the regions around a given point η in the ζ space by adding a biasing term to the potential of the atomic system such as $U_\eta(\zeta^t) = \frac{k}{2}(\zeta^t - \eta)^2$ in which ζ^t is the instantaneous value of collective variable ζ at time t and k is the force constant. The free energy of the biased system (or the perturbed free energy) $F(\eta)$ is:

$$e^{-\beta F(\eta)} = \int d\zeta e^{-\beta(G(\zeta)+U_\eta(\zeta))}. \tag{1}$$

Generalizing the formula in reference 10, one can show that the perturbed free energy at $F(\zeta)$ and the PMF $G(\zeta)$ are related via:

$$e^{-\beta G(\zeta)} \propto e^{-\frac{1}{2\beta k} \nabla_{\zeta}^2 e^{-\beta F(\zeta)}}. \quad (2)$$

For large k , i.e., in the stiff-spring approximation,¹¹ one may expand the above relation to extract the first two terms in $1/k$:¹⁰

$$G(\zeta) \approx F(\zeta) + \frac{1}{2\beta k} \left(\beta \nabla_{\zeta} F(\zeta) \cdot \nabla_{\zeta} F(\zeta) - \nabla_{\zeta}^2 F(\zeta) \right). \quad (3)$$

Thus, for large force constants, the PMF can be approximated using the perturbed free energy $F(\zeta)$. The validity of this approximation can be tested by *a posteriori* comparison of the two terms, assuming the gradient and Laplacian of the perturbed free energy are estimated as well—which is numerically challenging in a high-dimensional space.

Ideally, one may use a one-dimensional collective variable for defining the effective dynamics as well as the biasing protocol. In practice, however, this may only be possible for extremely simple systems. A practical solution to this problem is to keep the collective-variable space multidimensional, while sampling only around a particular pathway, represented by a one-dimensional curve $\zeta(s)$, parametrized by s . The choice of the pathway is obviously crucial here and determines the relevance of the free energy results to the transition of interest. Several path-finding algorithms have been proposed which iteratively/adaptively refine an initial pathway to converge to a final pathway satisfying a given criterion, *e.g.*, by minimizing the free energy or maximizing the flux.^{2,12–15} Among them is the string method with swarms of trajectories² which is used in this study.

Assuming $\zeta(s)$ approximately represents the minimum free-energy path, and s is its arc-length, relation (3) can be simplified to:

$$G\left(\zeta(s)\right) \approx F(s) + \frac{1}{2\beta k} \left(\beta \left(\frac{d}{ds} F(s) \right)^2 - \frac{d^2}{ds^2} F(s) \right), \quad (4)$$

in which $F(s)$ is, up to an additive constant, the free energy associated with the system perturbed by biasing potential $\frac{k}{2}(\zeta^t - \zeta(s))^2$, and $\frac{d^2}{ds^2} F(s)|_{s=s'} - \frac{d^2}{ds^2} F(s)|_{s=s''}$ is assumed to dominate $\nabla_{\zeta}^2 F(\zeta)|_{\zeta=\zeta(s')} - \nabla_{\zeta}^2 F(\zeta)|_{\zeta=\zeta(s'')}$. Under this assumption, the validation of the stiff-spring approximation requires the evaluation of $F(s)$ and its first and second derivatives with respect to the arc-length s . In order to numerically estimate $F(s)$, one may use umbrella sampling (US)¹⁶ to discretize s and define N umbrella windows/images with biasing potentials $U_i(\zeta^t) = \frac{k}{2}(\zeta^t - \zeta(s_i))^2$ for $i = 0, \dots, N - 1$. This scheme can be thought of as a one-dimensional US along the model reaction coordinate s with an additional restraint on the (shortest) distance from the $\zeta(s)$ curve. Perturbed free energies $F_i = F(\zeta(s_i))$ can be estimated (up to an additive constant) by self-consistently solving the equations:^{17,18}

$$e^{-\beta F_i} = \sum_t \frac{e^{-\beta U_i(\zeta^t)}}{\sum_j T_j e^{-\beta(U_j(\zeta^t) - F_j)}}, \quad (5)$$

in which \sum_t sums over all collected samples (irrespective of which replica or image they belong to) and T_j is the number of samples collected for image j .

With appropriate reweighting, the PMF can be reconstructed in any arbitrary collective variable space, given sufficient sampling in that space. w^t , the unnormalized weight of configuration \mathbf{x}^t can be estimated via:¹⁷

$$w^t = \left(\sum_i T_i e^{-\beta(U_i(\zeta^t) - F_i)} \right)^{-1} \quad (6)$$

in which $\{F_i\}$ are estimated via Equation (5). Alternatively,¹⁷ one may estimate $\{w^t\}$ and $\{F_i\}$ by iteratively solving Equation (6) and:

$$e^{-\beta F_i} = \sum_t w^t e^{-\beta U_i(\zeta^t)}. \quad (7)$$

The PMF in terms of $\xi(\mathbf{x})$, an arbitrary collective variable, is estimated (up to an additive constant) as:

$$G(\xi) = -\beta^{-1} \ln \left(\sum_t w^t \mathbf{K}(\xi(\mathbf{x}^t) - \xi) \right) \quad (8)$$

in which \mathbf{K} is a kernel function. The above estimator is not accurate if the sampling in $\xi(\mathbf{x})$ is not converged which is the case if $\xi(\mathbf{x})$ has a slow dynamics and is not strongly correlated with ζ . For the special case of $\xi = \zeta$, the perturbed free energies $\{F_i\}$ can be used directly to estimate the PMF in the stiff-spring approximation.

The maximum-likelihood (or maximum *a posteriori*) weighting scheme described above is general for any arbitrary set of biasing potentials; however, to approximate $G(\zeta(s_i))$ by $\{F_i\}$ and to examine the stiff-spring approximation by evaluation of the second term of the expansion in relation (4), and more importantly to relate $G(\zeta(s_i))$ to the kinetics even qualitatively, one needs to make an assumption that $\zeta(s_i)$ is an approximation of the minimum free energy path. Assuming the scheme results in a smooth function for $F(s)$, the first and second derivatives can be numerically estimated via finite difference methods from $\{F_i\}$ to evaluate the second term of the stiff-spring approximation.

Finally, for averaging an arbitrary quantity $A(\mathbf{x})$ along the pathway $\zeta(s)$, one may use the weighted average $\bar{A}(s) = \sum_t w^t A(\mathbf{x}^t) \delta(\zeta^t - \zeta(s))$. However, in the stiff-spring approximation, unweighted estimator $\bar{A}_i = \langle A(\mathbf{x}^t) \rangle_i$ is often more efficient. $\bar{\sigma}_i^2 = \langle A^2(\mathbf{x}^t) - \bar{A}^2 \rangle_i / g$ provides an estimate for the variance, given $g = 1 + 2\tau_{ac}^A / \Delta t$ is the statistical inefficiency in which τ_{ac}^A is the autocorrelation time associated with quantity A , and Δt is the lag time between the data points used in the analysis.¹⁹

Theoretical framework for rate estimation along the minimum free-energy path

Suppose that $\xi(\mathbf{x})$ is a one-dimensional coarse coordinate (or collective variable) defined as a function of atomic coordinates \mathbf{x} , and $G(\xi)$ is the potential of mean force associated with ξ ,

$$\exp\left(-\beta G(\xi)\right) = \left\langle \delta\left(\xi(\mathbf{x}^t) - \xi\right) \right\rangle, \quad (9)$$

in which $\langle \cdot \rangle$ is an ensemble average and $\beta^{-1} = k_B T$, in which T and k_B are the temperature and Boltzmann constant, respectively. Assuming ξ dynamics can be effectively described by a diffusive model, we have,

$$d\xi = \left(-\beta D(\xi) \frac{d}{d\xi} G(\xi) + \frac{d}{d\xi} D(\xi) \right) dt + \sqrt{2D(\xi)} dB. \quad (10)$$

in which $D(\xi)$ is a position-dependent diffusion constant, and $B(t)$ is a Wiener process such that $\langle B(t) \rangle = 0$ and $\langle B^2(t) \rangle = t$. The Fokker-Planck (or Smoluchowski) equation associated with this process is:²⁰

$$\frac{\partial}{\partial t} p(\xi, t | \xi_0, 0) = \frac{\partial}{\partial \xi} \left(D(\xi) \exp\left(-\beta G(\xi)\right) \right) \frac{\partial}{\partial \xi} \left(\exp\left(\beta G(\xi)\right) p(\xi, t | \xi_0, 0) \right), \quad (11)$$

in which $p(\xi, t | \xi_0, 0)$ is the likelihood of finding the system at ξ after time t , given it was at ξ_0 at time 0. Discretizing the above relation results in,

$$\mathbf{P}(\delta t) = (\mathbf{1} + \mathbf{R}\delta t)\mathbf{P}(0), \quad (12)$$

for small δt , in which $\mathbf{P}(t)$ is a vector with elements $P_i = p(\xi_i, t | \xi_0, 0)$, and \mathbf{R} is a tridiagonal matrix with elements:

$$R_{i i \pm 1} = \delta \xi^2 D(\xi_{i i \pm \frac{1}{2}}) \exp \left(-\beta \left(G(\xi_i) - G(\xi_{i \pm \frac{1}{2}}) \right) \right), \quad (13)$$

and $R_{i i} = -R_{i i+1} - R_{i i-1}$. More generally, for any lag time Δt and any time t , we have:

$$\mathbf{P}(t + \Delta t) = \exp(\mathbf{R}\Delta t)\mathbf{P}(t), \quad (14)$$

which indicates the likelihood of finding a trajectory at bin j at time $t + \Delta t$, given it was at bin i at time t , is proportional to $\exp(\mathbf{R}\Delta t)_{i j}$. Therefore, assuming that neither $G(\xi)$ nor $D(\xi)$ is known, one may find both, as in Ref. 21, by maximizing the likelihood $L = \prod_{\alpha} \exp(\mathbf{R}\Delta t)_{i_{\alpha} j_{\alpha}}$ (\prod_{α} runs over all observations of trajectories starting at the i_{α} at a given time t and being found at bin j_{α} at time $t + \delta t$). Assuming $G(\xi)$ is known, one may find $D(\xi)$ using a similar maximum-likelihood approach. For any given $D(\xi)$, \mathbf{R} can be evaluated, resulting in the log-likelihood,

$$l = \sum_{\alpha} \ln \left(\exp(\mathbf{R}\delta t)_{i_{\alpha} j_{\alpha}} \right), \quad (15)$$

which can be maximized using a Metropolis Monte Carlo algorithm. We first estimate the factors $\exp \left(-\beta \left(G(\xi_i) - G(\xi_{i \pm \frac{1}{2}}) \right) \right)$ in $R_{i i \pm 1}$ by evaluating the function $G(\xi)$ at $\xi = \xi_A + n \frac{\delta \xi}{2}$ for $n = 0, 1, \dots, 2N$, in which $G(\xi)$ is defined in the range $[\xi_A, \xi_B]$ and $N = \lceil \frac{\xi_B - \xi_A}{\delta \xi} \rceil$. An arbitrary series $D_{i+\frac{1}{2}}, i = 0, \dots, N-1$ can be used as an initial guess for $D(\xi_{i+\frac{1}{2}})$. $R_{i i \pm 1}$ and $R_{i i}$ values are then calculated to estimate the log-likelihood l . For a faster convergence, one may start with the estimates of \mathbf{R} associated with the $\Delta t \rightarrow 0$ limit of relation (13) (i.e., relation (12)) to maximize the log-likelihood in (15). It is easy to show that the following values for $R_{i, i \pm 1}$ maximize the

log-likelihood in (15) at the $\Delta t \rightarrow 0$ limit:

$$R_{i i \pm 1} = \frac{1}{\Delta t} \frac{N_{i i \pm 1} + N_{i \pm 1 i}}{N_{i i} \exp \left(-\beta \left(G(\xi_{i \pm 1}) - G(\xi_i) \right) \right) + N_{i \pm 1 i \pm 1}}, \quad (16)$$

in which N_{ij} is the number of observed jumps from bin i to j at the given lag time Δt . Diagonal values of \mathbf{R} can be also estimated as usual using $R_{ii} = -R_{i i+1} - R_{i i-1}$. while the other elements are zero. For an arbitrary lag time Δt , the log-likelihood in relation (15) can be evaluated using the values of N matrix as (for any given matrix \mathbf{R}):

$$l = \sum_{\alpha} N_{ij} \ln \left(\exp(\mathbf{R} \delta t)_{ij} \right). \quad (17)$$

Starting from the $\Delta t \rightarrow 0$ limit of \mathbf{R} , one can use a metropolis Monte Carlo algorithm to maximize the log-likelihood l in relation (17). $D_{i+\frac{1}{2}}$ is then can be estimated using:

$$D_{i+\frac{1}{2}} = \delta \xi^2 R_{i i+1} \exp \left(\beta \left(G(\xi_i) - G(\xi_{i+\frac{1}{2}}) \right) \right). \quad (18)$$

$D(\xi_i)$ can be estimated by interpolation $(D_{i-\frac{1}{2}} + D_{i+\frac{1}{2}})/2$. The mean-first-passage time $\bar{\tau}_{FP}$ (i.e., the rate inverse, k^{-1}) from the initial (A) to the final (B) state can be then estimated using the following relation:²²

$$k^{-1} = \bar{\tau}_{FP} = \int_{\xi_A}^{\xi_B} d\xi \frac{\int_{\xi_A}^{\xi} d\xi' \exp \left(-\beta G(\xi') \right)}{D(\xi) \exp \left(-\beta G(\xi) \right)}. \quad (19)$$

k and $\bar{\tau}_{FP}$ were estimated numerically using:

$$k^{-1} = \bar{\tau}_{FP} = \sum_{i=0}^N \frac{\sum_{j=0}^i \exp \left(-\beta G(\xi_j) \right)}{D(\xi_i) \exp \left(-\beta G(\xi_i) \right)}. \quad (20)$$

Estimating the number of observed jumps from image i to j within a time interval Δt (i.e., lag time), we can build a (Δt dependent) matrix N_{ij} , which contains all the information needed to estimate the \mathbf{R} .²³ Using relation (16), we can estimate an initial value for the \mathbf{R} elements (Figure S9a). The log-likelihood l is calculated using relation (17). At every iteration, an R_{ij} value (conditioned on $i = j \pm 1$) is randomly selected and altered by adding a random number ϵ between $-0.05/\Delta t$ and $0.05/\Delta t$. This will require the modification of three other non-zero elements of \mathbf{R} immediately neighboring R_{ij} according to $R'_{ji} = R_{ji} + \epsilon \exp\left(-\beta(G(\xi_j) - G(\xi_i))\right)$, $R'_{ii} = R_{ii} - \epsilon \exp\left(-\beta(G(\xi_j) - G(\xi_i))\right)$, and $R'_{ii} = R_{ii} - \epsilon$. These modification will be accepted with the probability $\min(1, \exp(l' - l))$, in which l and l' are the old and new log-likelihoods calculated using (17). The algorithm will stop once the log-likelihood converges within a given numerical accuracy ($|l' - l| < X$) (Figure S9b). $D_{i+\frac{1}{2}}$ is then can be estimated using relation (18) with $\delta\xi = 1$. $D(\xi_i)$ can be estimated by interpolation $(D_{i-\frac{1}{2}} + D_{i+\frac{1}{2}})/2$.

All the VMD and NAMD tcl-scripts required for implementation of the aforementioned free-energy and rate methods, as well as those for the string simulations are provided herewith in a separate folder, denoted **Simulation-script**.

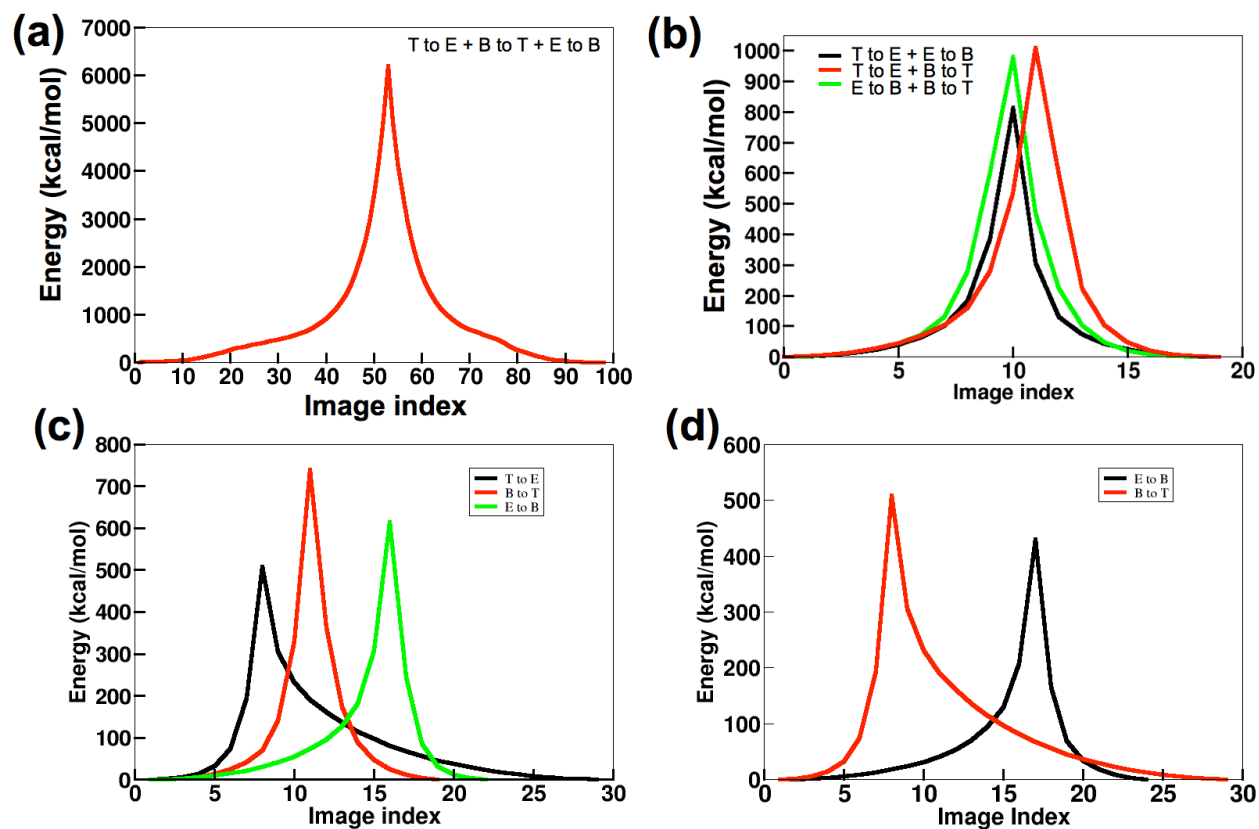


Figure S3: The energy changes from Anisotropic Network Model (ANM)-predicted pathways of conformational transitions in the V_1 -ring (A_3B_3) complex are employed to screen the most probable sequence of events that connect R^* to F^* . (a) First, all the three protein states are allowed to change simultaneously in an ANM pathway: ($A^eB^e, A^tB^t, A^bB^b \rightarrow A^bB^b, A^eB^e, A^tB^t$). (b) Second, two protein states change simultaneously during ANM: ($A^eB^e, A^tB^t, A^bB^b \rightarrow A^bB^b, A^eB^e, A^bB^b$), ($A^eB^e, A^tB^t, A^bB^b \rightarrow A^bB^b, A^tB^t, A^tB^t$), ($A^eB^e, A^tB^t, A^bB^b \rightarrow A^eB^e, A^eB^e, A^tB^t$). (c) Third, only one state changes at a time: ($A^eB^e, A^tB^t, A^bB^b \rightarrow A^bB^b, A^tB^t, A^bB^b$), ($A^eB^e, A^tB^t, A^bB^b \rightarrow A^eB^e, A^eB^e, A^bB^b$), ($A^eB^e, A^tB^t, A^bB^b \rightarrow A^eB^e, A^tB^t, A^tB^t$). (d) The product from the pathway with the lowest barrier among the seven ANM pathways, (A^eB^e, A^eB^e, A^bB^b), was subjected to two further transitions ($A^eB^e, A^eB^e, A^bB^b \rightarrow A^bB^b, A^eB^e, A^bB^b$) and ($A^eB^e, A^eB^e, A^bB^b \rightarrow A^eB^e, A^eB^e, A^tB^t$); the former pathway exhibits a smaller barrier.

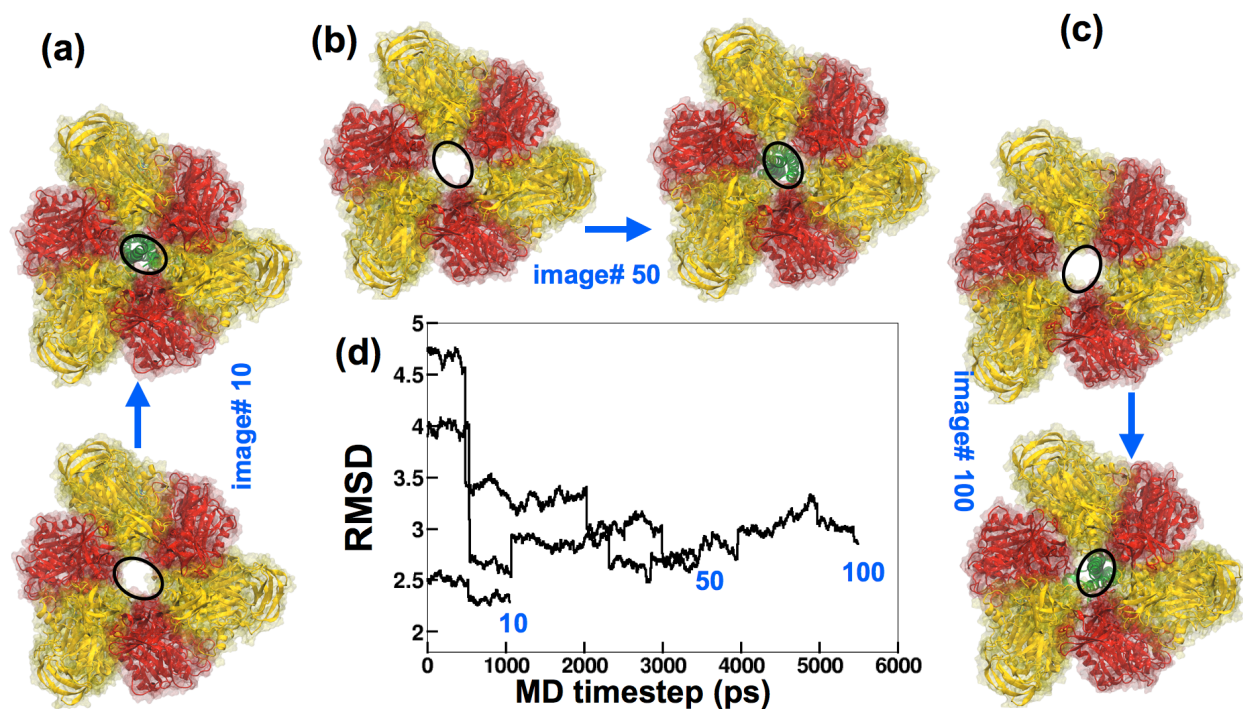


Figure S4: Protocol for generating a trial pathway of conformational transitions in the V₁-rotor. Starting with structures along the minimal free energy pathway (MFEP) of the V₁-ring conformational rotation (Figure 3), V₁-rotor models are constructed for 100 images across the transition pathway via insertion of a DF stalk into the central pore of the respective rings. Structures representing image number 10 (a), 50 (b) and 100 (c) are provided before and after the stalk insertion. At each image, the insertion is realized with MDFF simulations of the central stalk into the density of the central pore, while simultaneously performing TMD simulations that constrains the ring of the V₁-rotor to conformations along the V₁-ring MFEP derived in Figure 3. (d) Convergence of the combined TMD and MDFF procedure is shown for selected images in terms of RMSD of structures from the V₁-rotor pathway with respect to those from their target along the V₁-ring pathway. For a given image, the initial decrease in RMSD confirms that TMD has enforced a ring conformation within the V₁-rotor, which is similar to that from the V₁-ring rotation pathway at the particular point. However, convergence to RMSD values of 2 to 3 Å implies that insertion of a stalk still changes the local structure of the ring, and the V₁-rotor and V₁-ring conformational transition pathways are disparate. Since the TMD simulation for constructing the I→F pathway for the V₁-rotor structural transition is initiated with a structure representing state I, convergence of this simulation for constructing images further away from I requires additional simulation time.

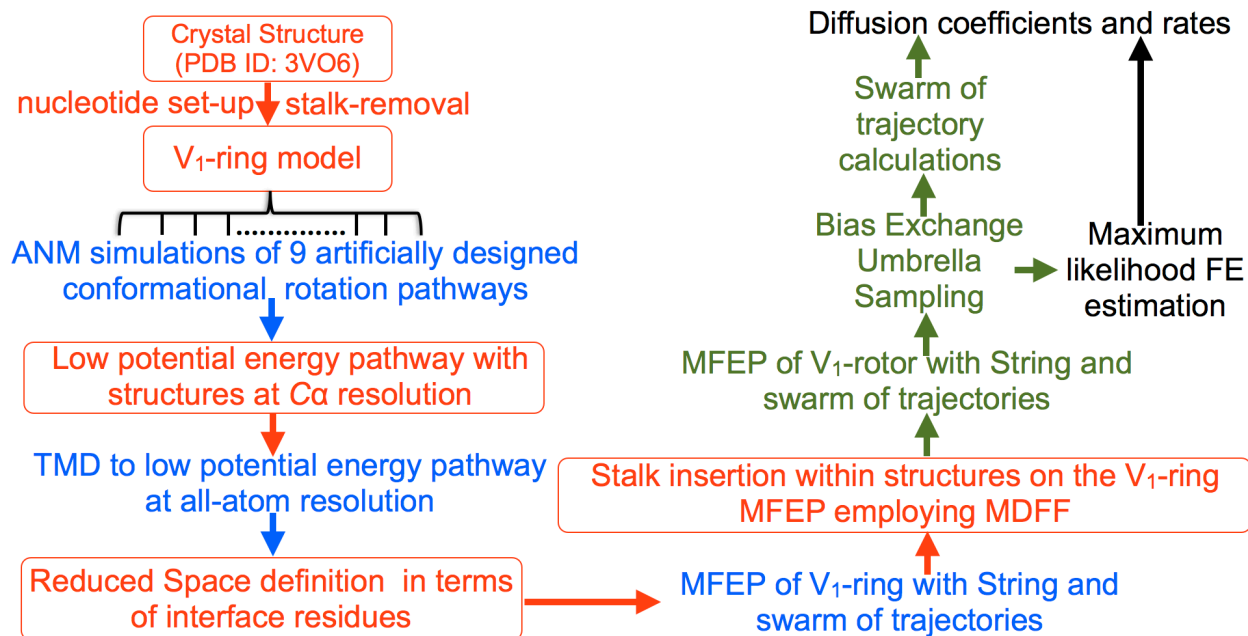


Figure S5: Workflow illustrating the computational protocol employed to capture the conformational transition pathways of the V_1 -ring and V_1 -rotor. The molecular modeling steps are indicated in red, the simulation steps in blue, and the analysis steps in black. The simulations begin with the setting of the nucleotide (ATP and ADP+P_i) states guided by FEP calculations. Nine ANM pathways are subsequently constructed for capturing the conformational rotation of the V_1 -ring. The pathway with the lowest barrier is refined via TMD and string simulations with swarm of trajectories to derive the MFEP for V_1 -ring conformational rotation. MDFF simulations are applied in concert with TMD simulations to construct a preliminary stalk rotation pathway that is further refined via a second round of string simulations. The resulting pathway is characterized for free-energy and rates by employing maximum-likelihood schemes with statistics acquired from BEUS and multi-copy MD simulations respectively.

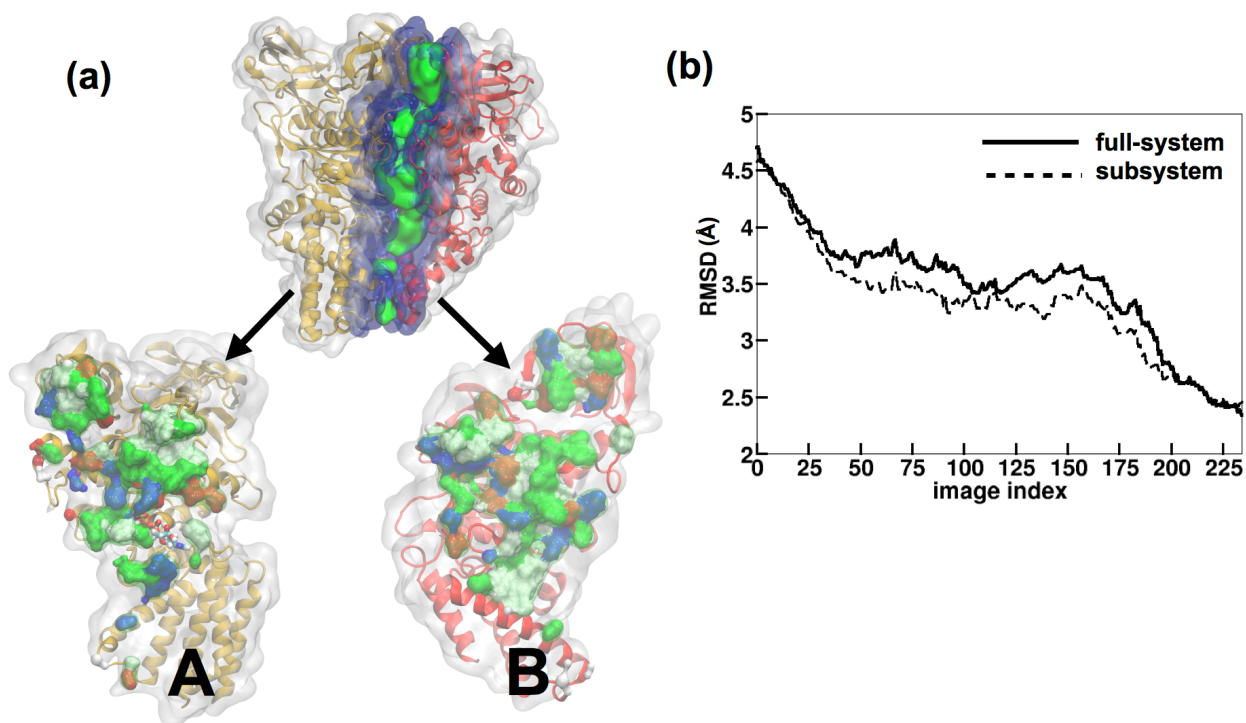


Figure S 6: Construction of the reduced space for the string simulations of the V₁-ring complex, as well as the V₁-rotor. (a) The nucleotide-containing AB interface is colored by interaction energies showing residues in green within a 10 Å cutoff contributing predominantly to the interface interactions. (b) The same set of residues capture the major RMSD changes within a tentative R* to F* pathway, thus, implying their significance in deriving a reduced description that probes the R* to F* conformational transition; the RMSD is computed with respect to the thermally-averaged F* structure. 84 residues are derived from the nucleotide-binding AB interface. An additional 47 residues are derived from the non-nucleotide binding interface. In total, the C-alpha atoms from each of these $3 \times (84+47)$ residues are considered to construct the $3 \times (84+47) \times 3 = 1179$ dimensional reduced space. The A subunit residues included in the subspace are number 7 8 9 10 11 12 54 55 56 57 58 59 60 61 62 83 85 91 92 94 95 101 102 103 104 105 233 234 235 260 261 262 263 264 265 266 267 268 270 271 293 294 295 296 297 298 299 300 333 336 337 340 343 344 346 347 352 353 392 393 from the chains A, B and C in the PDB file of the V₁-rotor, and similarly for the B subunit are residue numbers 23 24 25 26 27 46 47 48 49 76 114 115 116 117 118 119 120 121 122 123 124 144 145 146 266 267 269 270 275 276 278 279 282 283 286 287 289 317 320 321 322 323 324 350 351 from chains D, E and F.

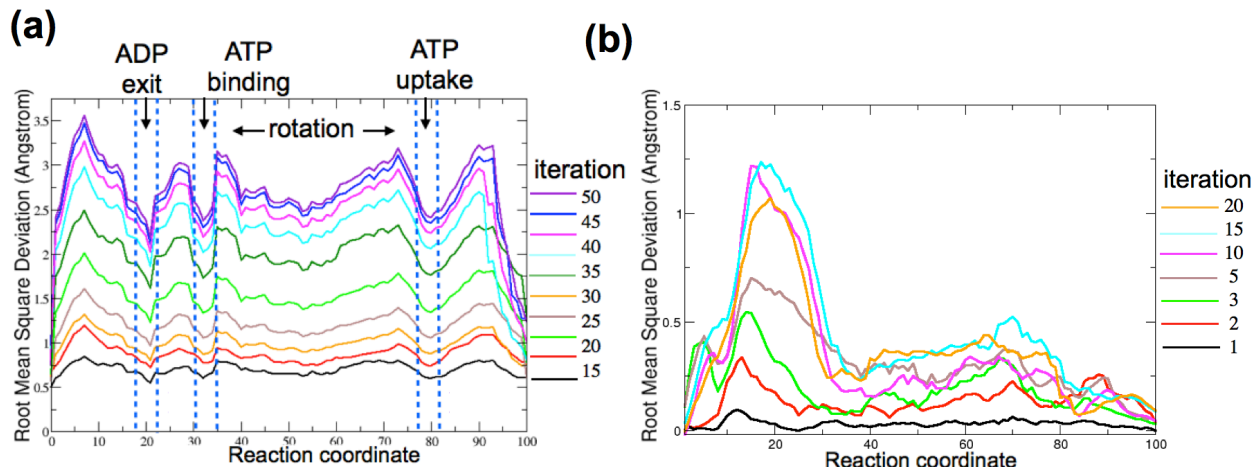


Figure S7: (a) RMSD drift of individual images from their initial configuration on the V_1 -ring conformational rotation pathway across 50 iterations of the string procedure showing that the drift ceases beyond 40 iterations and the string converges by 50 iterations, relaxing the trial pathway into a MFEP. (b) Similarly, for the V_1 -rotor stalk rotation pathway, only 20 more iterations are required within which the RMSD drift ceases beyond the first ten iterations.

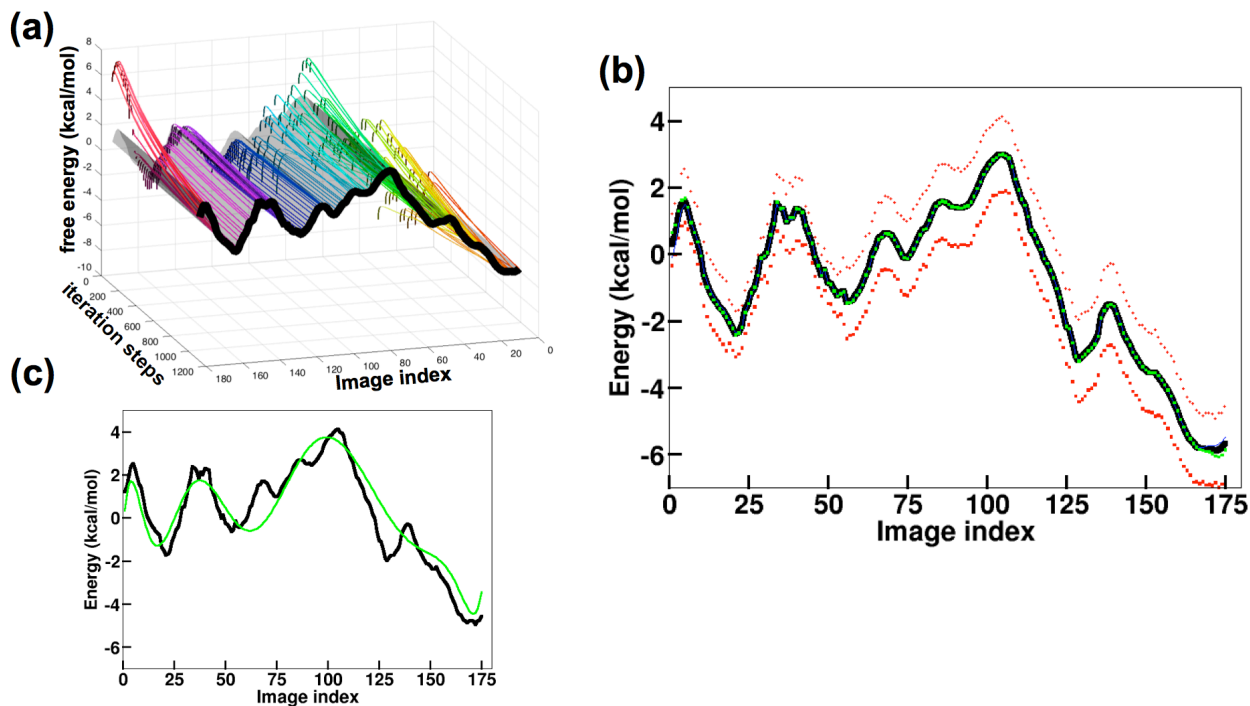


Figure S8: (a) Estimate of the free energy derived from statistics accumulated during the BEUS simulations across 175 images of the V_1 -rotor transition pathway. 1000 iterations of the maximum-likelihood scheme involving equations (6) and (7) suffice to provide a convergent one-dimensional free-energy profile. (b) The error estimation, performed using a resampling approach²⁴ with 100 trials, confirms that the free energy profile is computed with a sampling error of ± 1.5 kcal/mol. The free energy profile after the addition of higher order terms in equation (4), shown in green, changes negligibly. (c) An 11-th order polynomial approximation is derived out of the free-energy profile to derive the higher-order correction terms in equation (4).

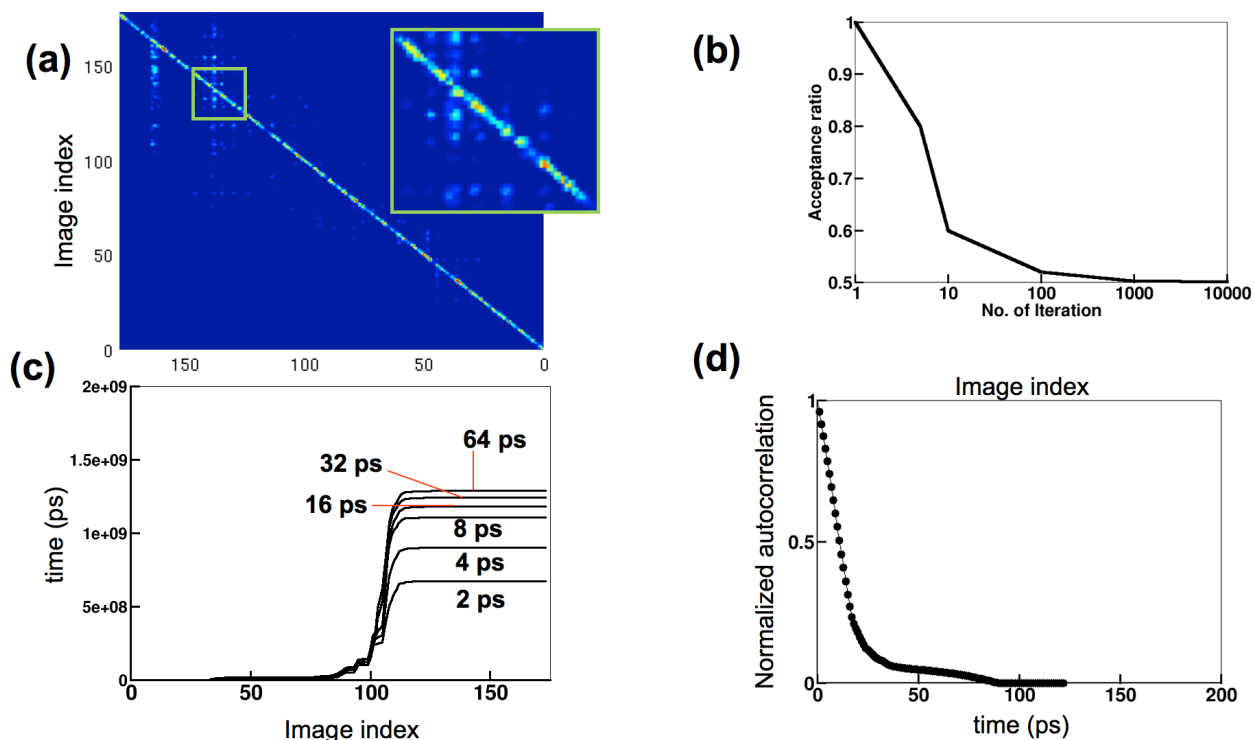


Figure S9: (a) The matrix N_{ij} (equation 16), illustrating the number of passages of unbiased MD trajectories between images i and j , is found to be block-diagonal. This feature implies that a reactive trajectory on the MFEP of the V_1 -rotor traverses primarily within immediate neighbors. (b) The acceptance ratio of the Metropolis–Hastings algorithm for the determination of diffusion coefficient by maximizing the log-likelihood (17) converges to 50% within 10,000 iterations. (c) The diffusion coefficient, and hence the first passage time $\bar{\tau}_{FP}$ (equation (20)) attributed to a conformational transition depends on the lag time, Δt , chosen to count the number of $i \rightarrow j$ passages in the matrix N_{ij} , and performing the subsequent maximum-likelihood analysis with equation (16). At smaller time intervals, the data remains correlated and therefore, the diffusion coefficient is overestimated, underestimating the transition time. The computed $\bar{\tau}_{FP}$ increases and converges to approximately 1.09 ms when the Δt is raised from 2 ps to 64 ps in powers of 2. (d) Autocorrelation function of the image index time series exhibits a decay time of 68 ps, in excellent agreement with the lag time of 64 ps used to construct the N_{ij} matrix, thus supporting our choice of Δt .

Results

Table S3: RMSD of the A and B proteins from the V_1 -ring as they undergo a conformational rotation from $I^* \rightarrow R^*$ and $I \rightarrow R$ states, elucidating that the magnitude of the change in the ring is comparable both in the presence and absence of the DF stalk. For a given change in the nucleotide binding site, i.e., between (e), (b) and (t), transformation of the B domains is mostly lesser than that of the A domains. Nonetheless, the B domain changes significantly during the $I^* \rightarrow II$ (Figure 3) and $I \rightarrow 2$ (Figure 5), where an empty site (B^{e*} or B^e) is transformed into bindable site ($B^{e*/}$ or $B^{e'}$) to facilitate ATP binding.

Transition	RMSD (Å)	Transition	RMSD (Å)
$A^{e*} \rightarrow A^{t*}$	2.5	$A^e \rightarrow A^t$	2.5
$A^{e*} \rightarrow A^{b*}$	2.2	$A^e \rightarrow A^b$	2.3
$A^{b*} \rightarrow A^{t*}$	1.7	$A^b \rightarrow A^t$	1.9
$A^{e*} \rightarrow A^{e*/}$	1.2	$A^e \rightarrow A^{e'}$	1.8
$B^{e*} \rightarrow B^{t*}$	2.1	$B^e \rightarrow B^t$	2.4
$B^{e*} \rightarrow B^{b*}$	1.7	$B^e \rightarrow B^b$	2.2
$B^{b*} \rightarrow B^{t*}$	1.2	$B^b \rightarrow B^t$	1.8
$B^{e*} \rightarrow B^{e*/}$	2.2	$B^e \rightarrow B^{e'}$	2.0

Table S4: List of hotspot residues identified employing Robetta computational alanine mutations of structures extracted from the string simulation of the V_1 -rotor. Mutations indicated by * are experimentally verified;^{25,26} the mutation indicated by + is observed from an intermediate, namely 2 in the V_1 -rotor transition pathway. This mutation is obscure to the end-points of the transition but is now identified in our simulations and validated by independent experiments.²⁵ The upper panel indicates key residues at the AD and BD interfaces, while the lower panel indicates those for the AB interface.

Subunit	Resid	$\Delta\Delta G_{\text{complex}}$ (kcal/mol)	$\Delta G_{\text{partner}}$ (kcal/mol)
*+A	396	1.20	0.92
*A	476	0.48	0.74
*A	477	0.33	0.65
B	270	3.21	0.15
B	271	1.43	0.08
D	11	1.07	0.12
+D	14	1.69	1.07
*D	28	0.81	0.81
D	161	1.15	0.56
D	165	1.95	0.44
A	300	0.06	1.08
A	303	6.56	5.27
A	333	2.03	1.15
A	352	1.27	1.55
B	221	3.94	6.21

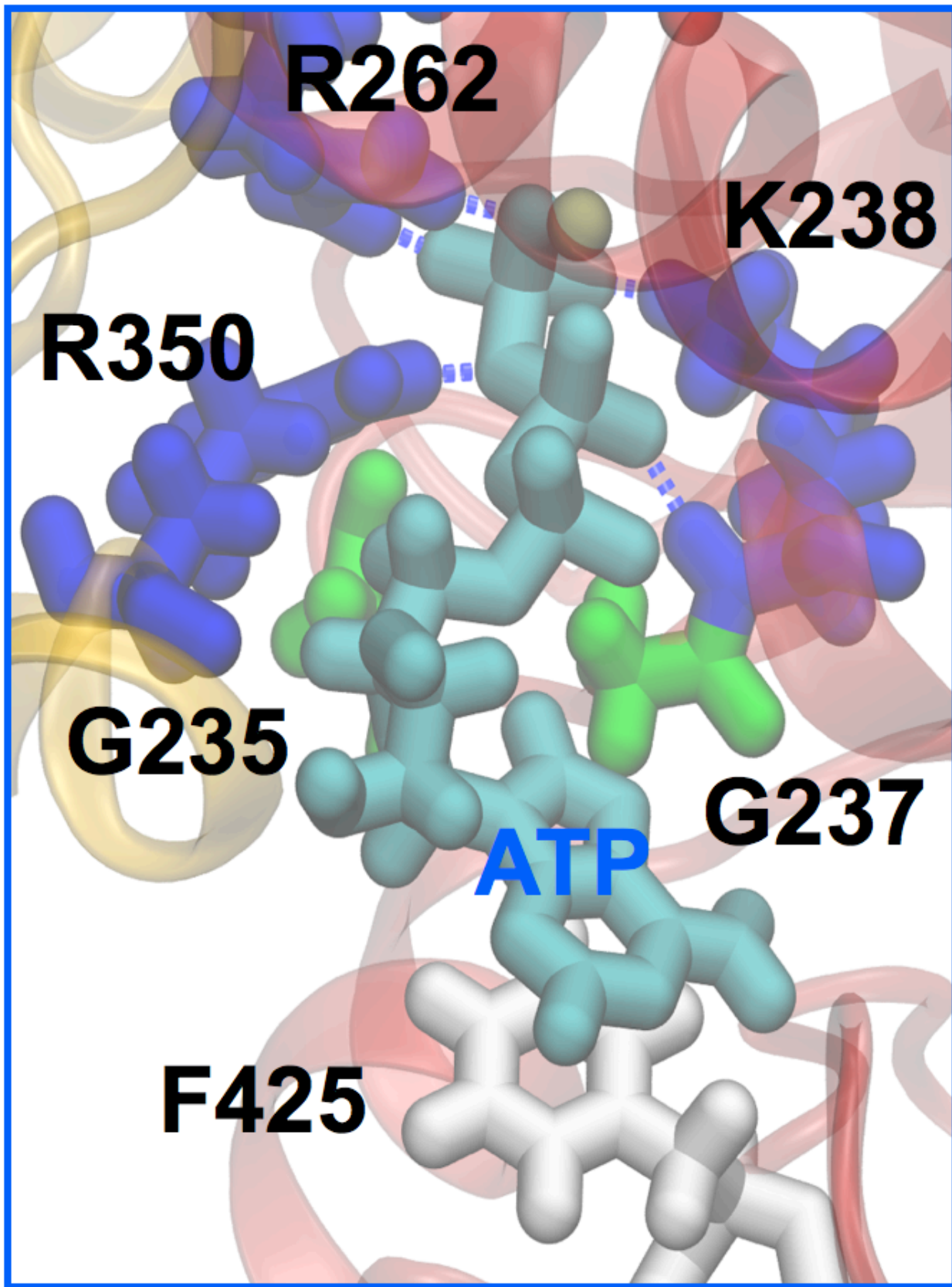


Figure S10: Close-up of the ATP binding pocket in the A subunit of the V₁-ring, highlighting key residues interacting with ATP's adenine base and the charged phosphate groups.

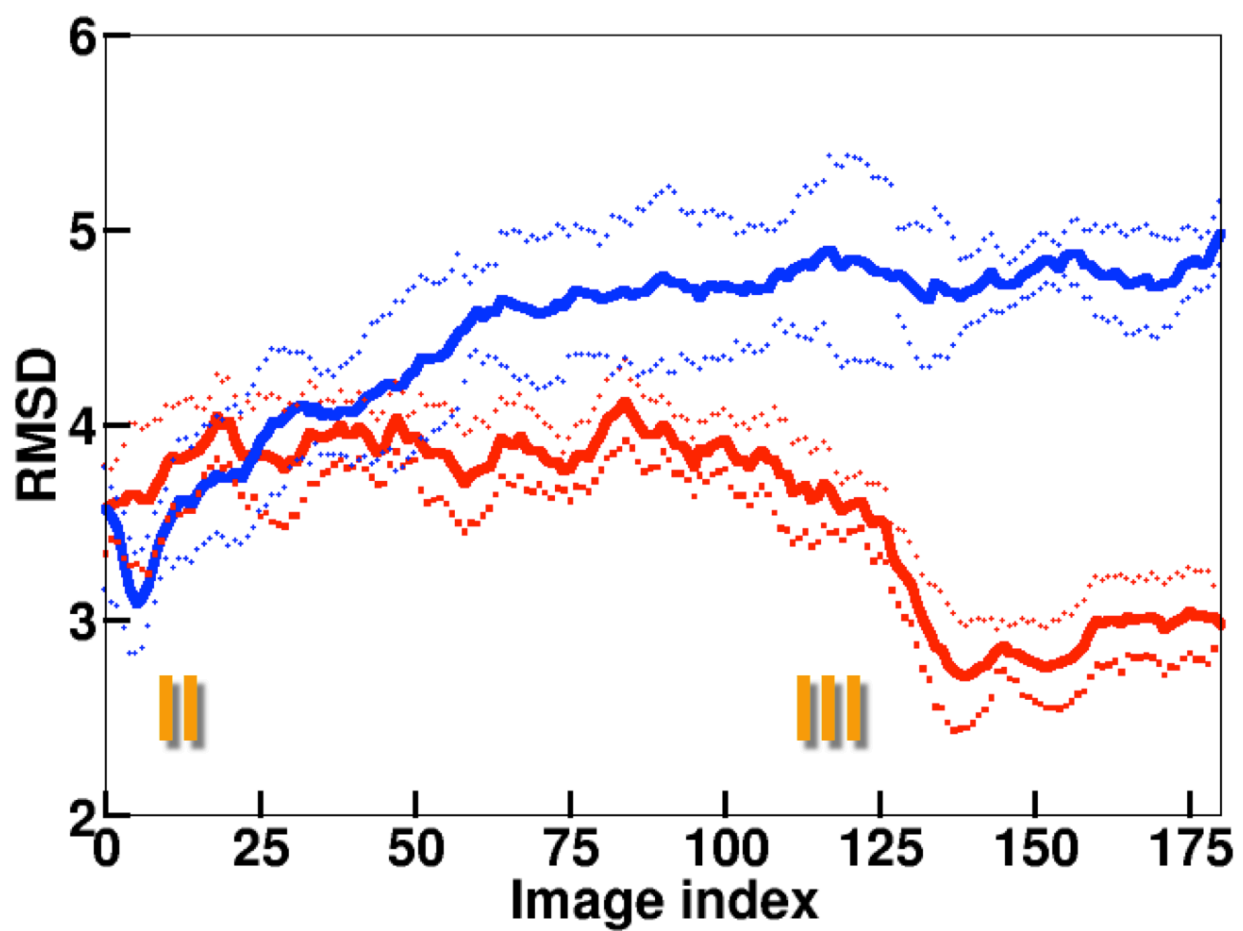


Figure S11: RMSD of the structures isolated along every image of the string simulation with respect to known crystal structures of V_1 -ring intermediates showing the intermediate II visits the **bi,e,b** state reported in PDB ID 3VR2, and intermediate III resembles state **b,e,b** of PDB ID 3VR3.

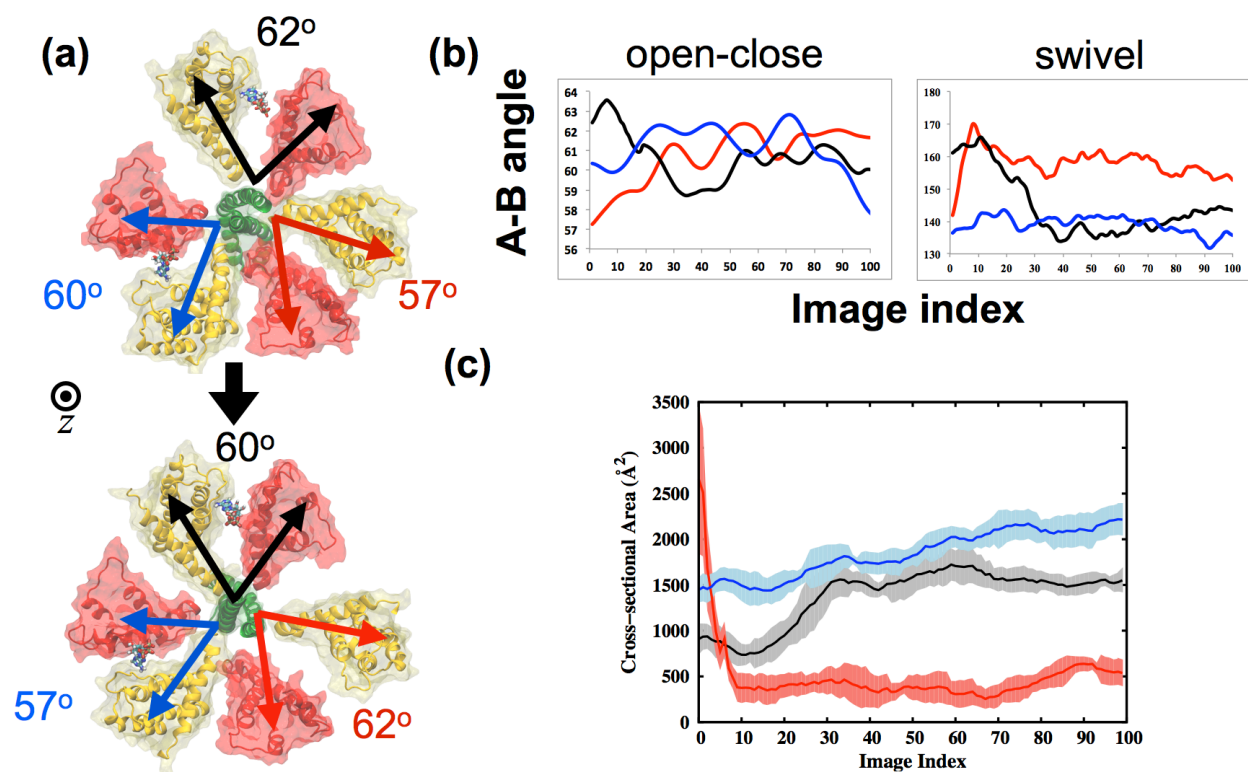


Figure S12: (a) Top-down view of the V₁-rotor highlighting angles between the A and B subunit at the nucleotide-binding interface along the XY coordinate plane, which captures opening and closing of the interface during the I → F structural transition. Hinge angle within the A subunit, perpendicular to the XY plane, which captures a swivel motion of the subunit is provided in Figures 9-10. (b) These angles, capturing the in and out-of-plane motions, are plotted along the I → F transition pathway, portraying clearly a series of events: opening of the A^tB^t interface, indicated by an increase in both the angles (red trace), is followed by a closing of A^eB^e shown by decrease in the associated angles (black trace) which, in turn, is followed by a closing of A^bB^b (blue trace). (c) The same sequence of events is captured by changes in the contact area of the AB interface, measured by methods presented in Ref 27. An opening of the A^tB^t interface, indicated by a decrease in contact area (red trace), is followed by an increase in the contact area of the A^eB^e interface (black trace), which, again, is followed by a closing of A^bB^b (blue trace).

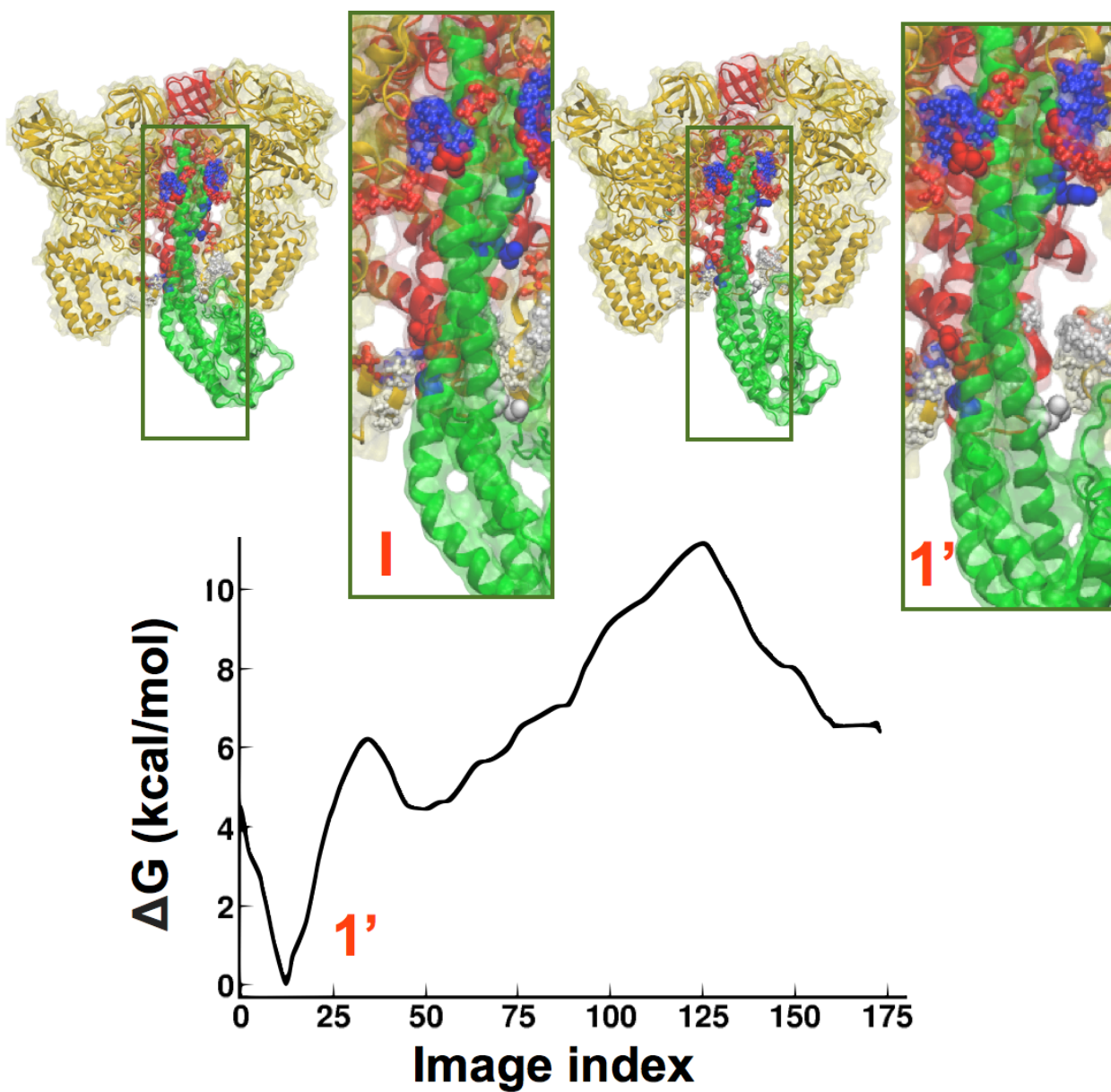


Figure S13: One-dimensional free energy profile characterizing the product (ADP + P_i)-inhibited pathway of V_1 -rotor structural transitions reveals that this process is endothermic, and that the rotation is thermodynamically unfavorable in the presence of products bound to the empty site. An intermediate is observed along this pathway, denoted 1', which resembles the A_3B_3 conformation of state I, but the stalk has straightened (inset).

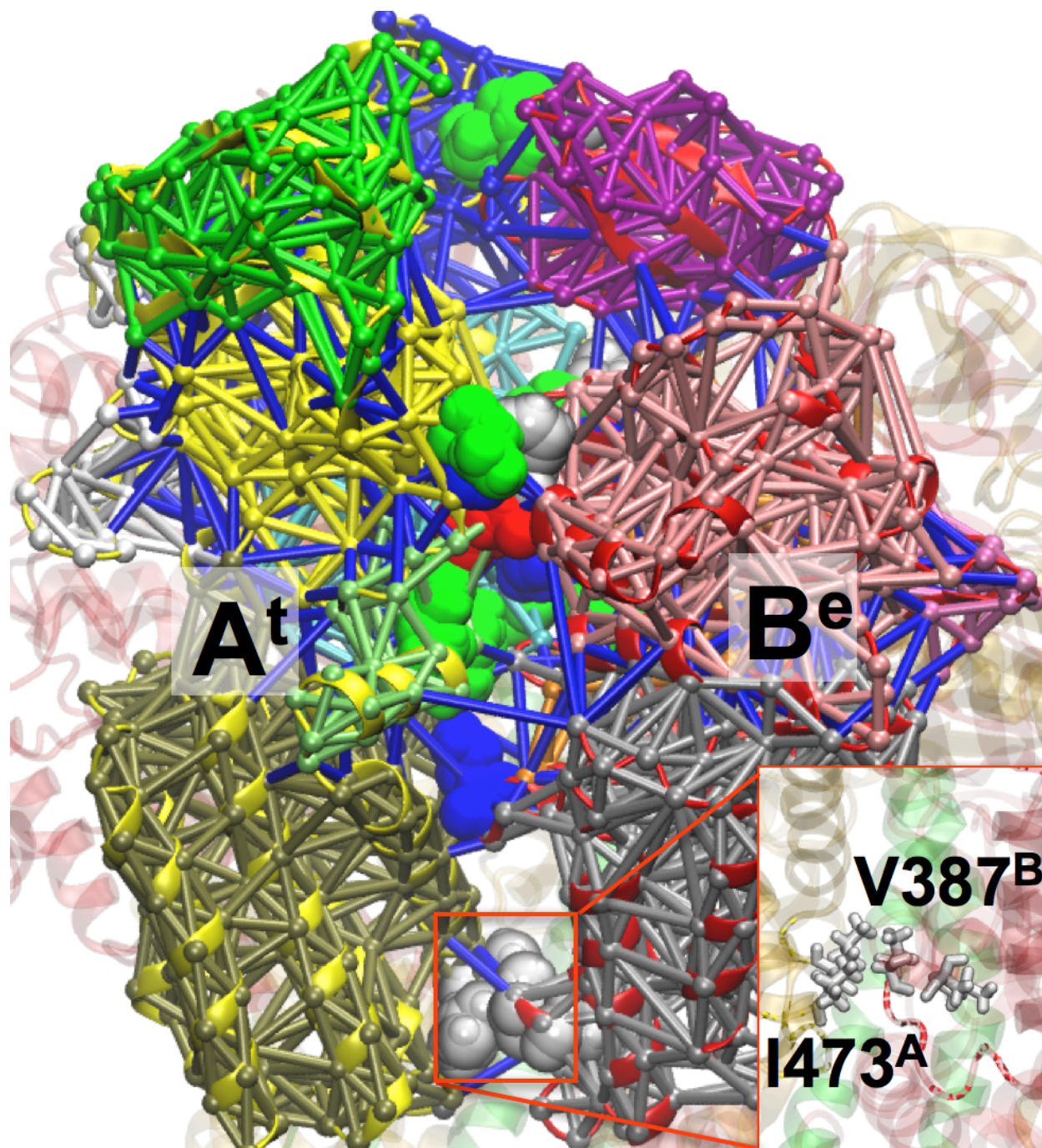


Figure S14: Dynamical network analysis of the $A^t B^e$ interface illustrating that the motion of hydrophobic residues I473 from the A domain and that of V387 from the B domain are dynamically correlated. (inset).

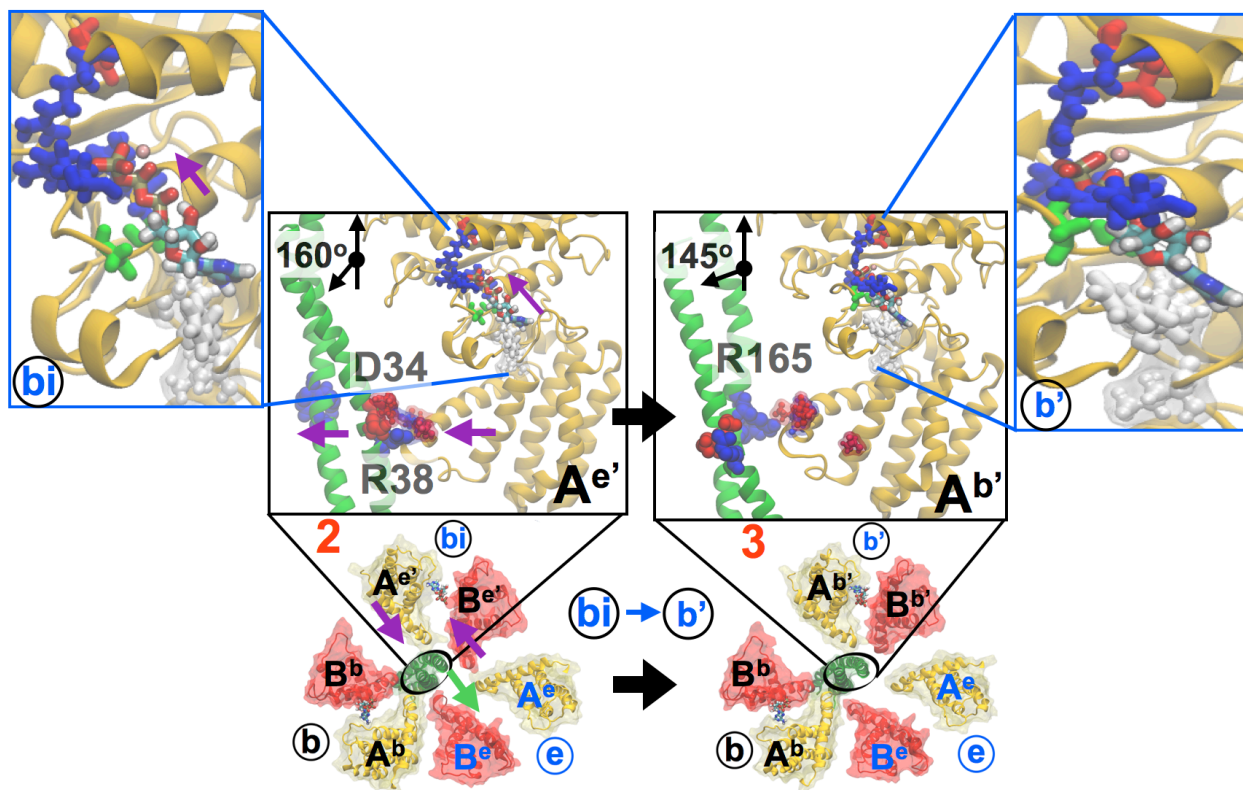


Figure S15: **Ring-stalk allostery: 2 → 3 transition.** Inward swivel of the A domain by 15° during the $A^{e'} \rightarrow A^{b'}$ transition is allosterically coupled to the motion of F425 in the ATP binding pocket (inset), in converse to the events present in Figure 9: as ATP crawls into the bindable site, F425 forms a π - π stacking interaction with the adenine base, which is accompanied by an inward swiveling motion of the $A^{e'}$. Simultaneously, D34 and R38 of the stalk lose electrostatic interactions with R475 and E472 of transformed $A^{b'}$, and R164 from the stalk starts interacting with the dangling E472. This reorganization induces a wringing deformation of the stalk. For the sake of clear presentation only stalk residues are labeled in the figure; all key residues at the ring-stalk interface are illustrated in Figure S16.

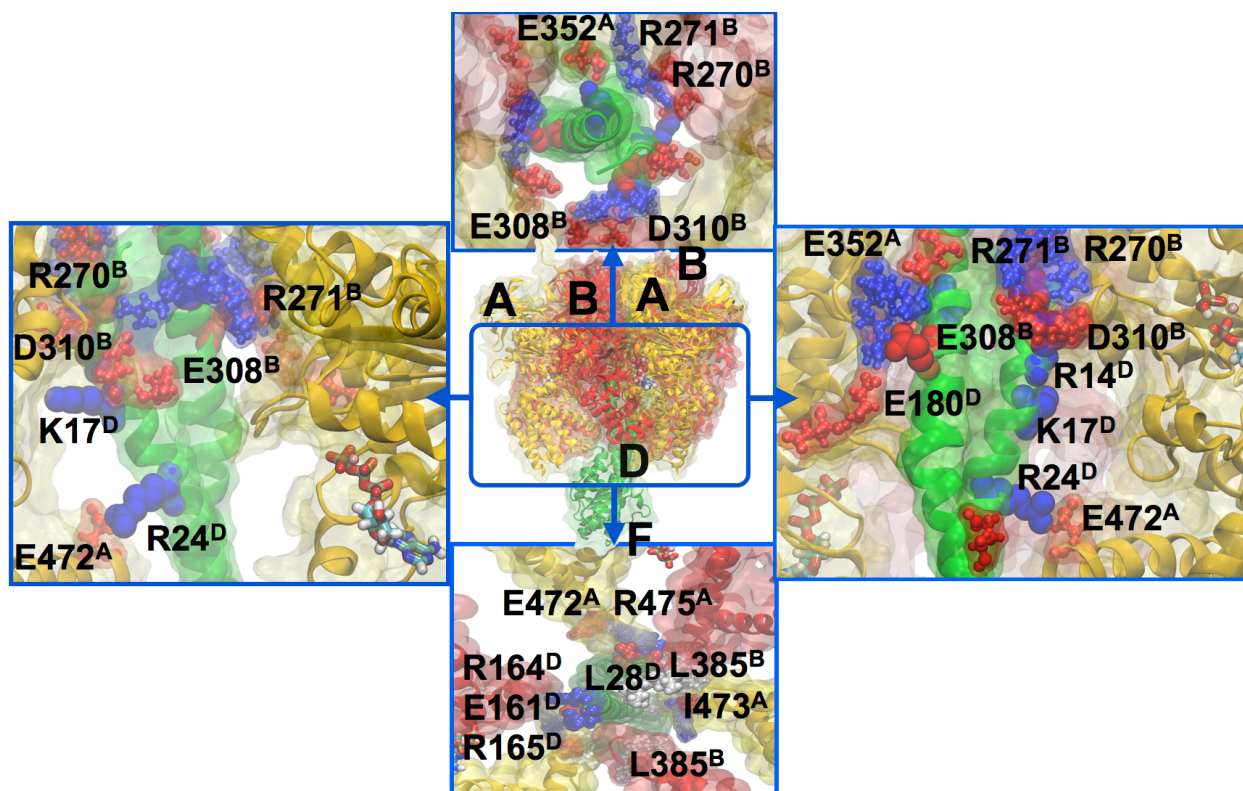


Figure S 16: Four views of the V₁-ring - DF stalk interface are presented in clockwise direction: top-down, transverse-section, top-down of a central slice and inverse transverse-section showing key residues that mediate rotation of the stalk. The same views are employed to showcase details of the rotational transition in movies M1 to M4. An additional movie, M5, is provided, which illustrates the wring and rotation of the entire stalk.

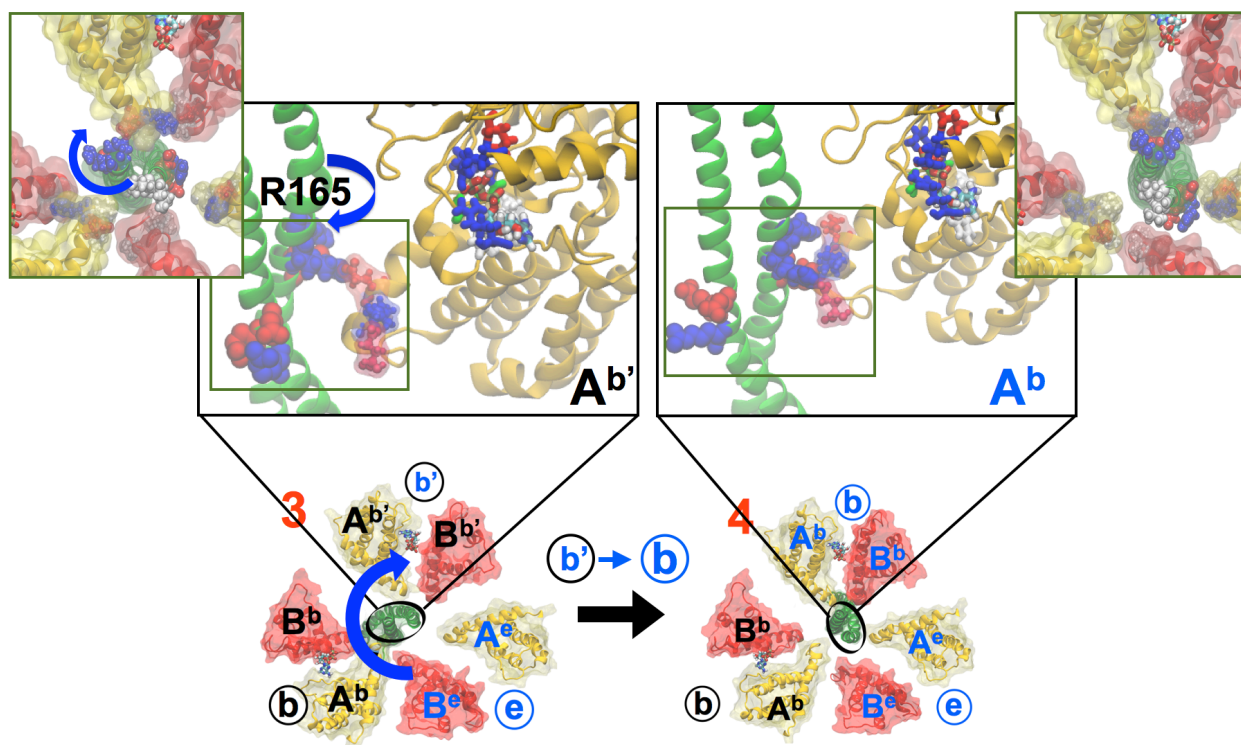


Figure S17: **Ring-stalk allostery: 3 \rightarrow 4 transition.** Rotation of the DF stalk involving the reorganization of the E161, R164 and R165 residues to allow interaction with R475 of the A^b subunit, E384 of B^b subunit and E472 of the A^b subunit.

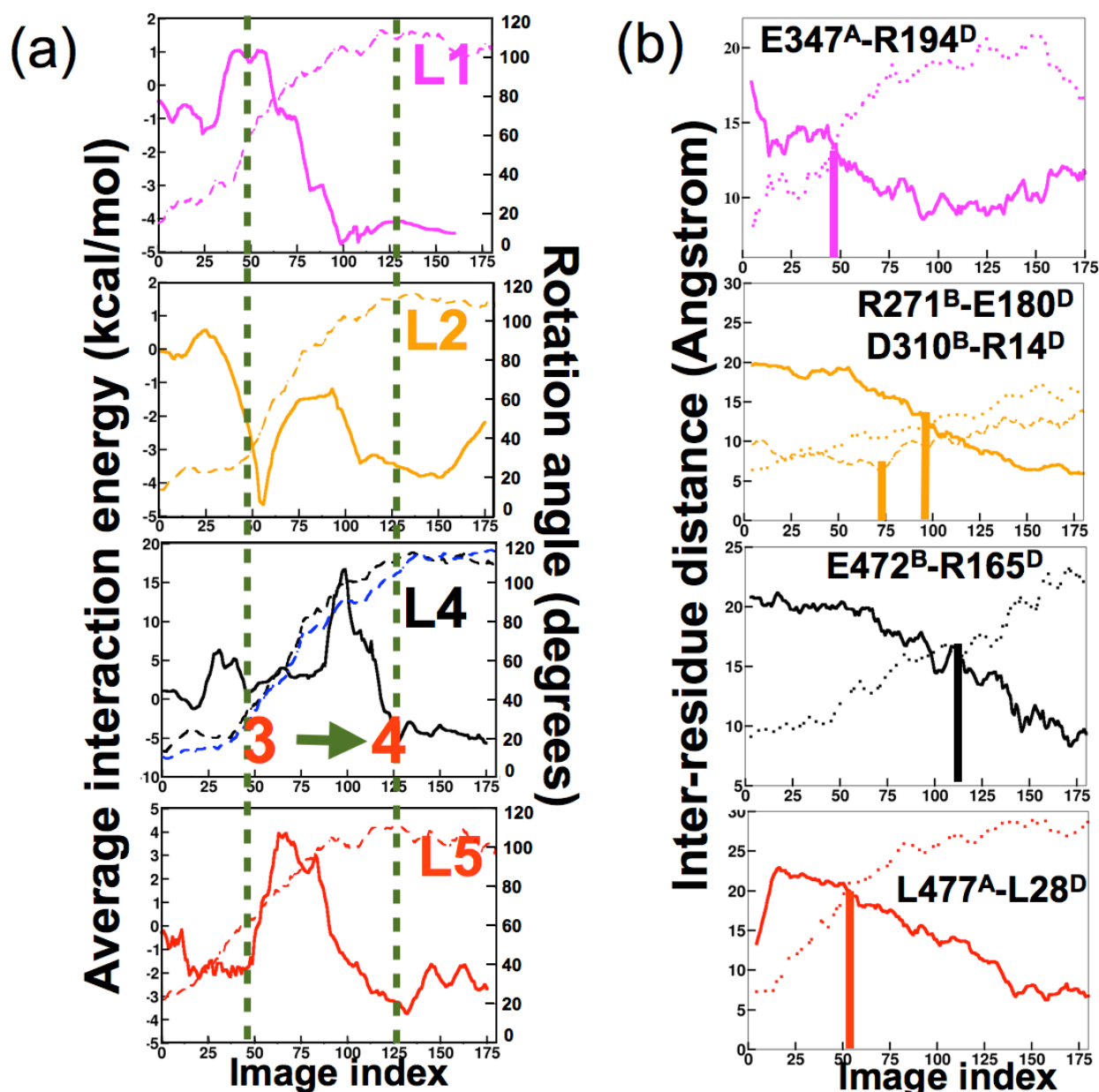


Figure S18: (a) Average interaction energies derived from the BEUS simulations (presented in solid lines) of layers L1 (purple), L2 (orange), L4 (black) and L5 (red) of the central stalk are presented along the transition path as functions of the image indices, and show that each layer overcomes a different magnitude of energy barrier and at different instant of time to manifest the overall rotation of the central stalk. Consequently, the change in rotation angle (presented in dotted lines) is observed over different range of images for different layers. While for the more flexible layers L1 and L5, the rotation happens earlier in the transition, also reflected in the wringing motion, rotation of L2 follows, and finally L4 rotates, overcoming the highest barrier. The rotation of layer L2 is initially slow as it conforms to a local energy minimum; its motion enhances subsequently due to structural coupling with the neighboring layer, L1, which rotates significantly over the same range of images to achieve a lower energy. L3, the layer with maximum torsional stiffness (Figure 8), shows minimal energy barriers as it is the least V_1 -ring-interacting part of the DF stalk. Therefore rotation of L3 (shown in blue dotted lines) remains inherently coupled to that of L4, the layer with the highest rotational barrier, as can be observed from the similarity in L3 and L4 rotational trends. (b) Primary interactions that contribute to the rotational barriers presented in (a) are shown in terms of the distance between respective partners. Dotted lines represent disruption of the ring-stalk interaction between residues from the A or B subunit and those from D; solid lines represent the recovery of these interactions after the stalk has rotated and new A-D or B-D interactions have been resurrected.

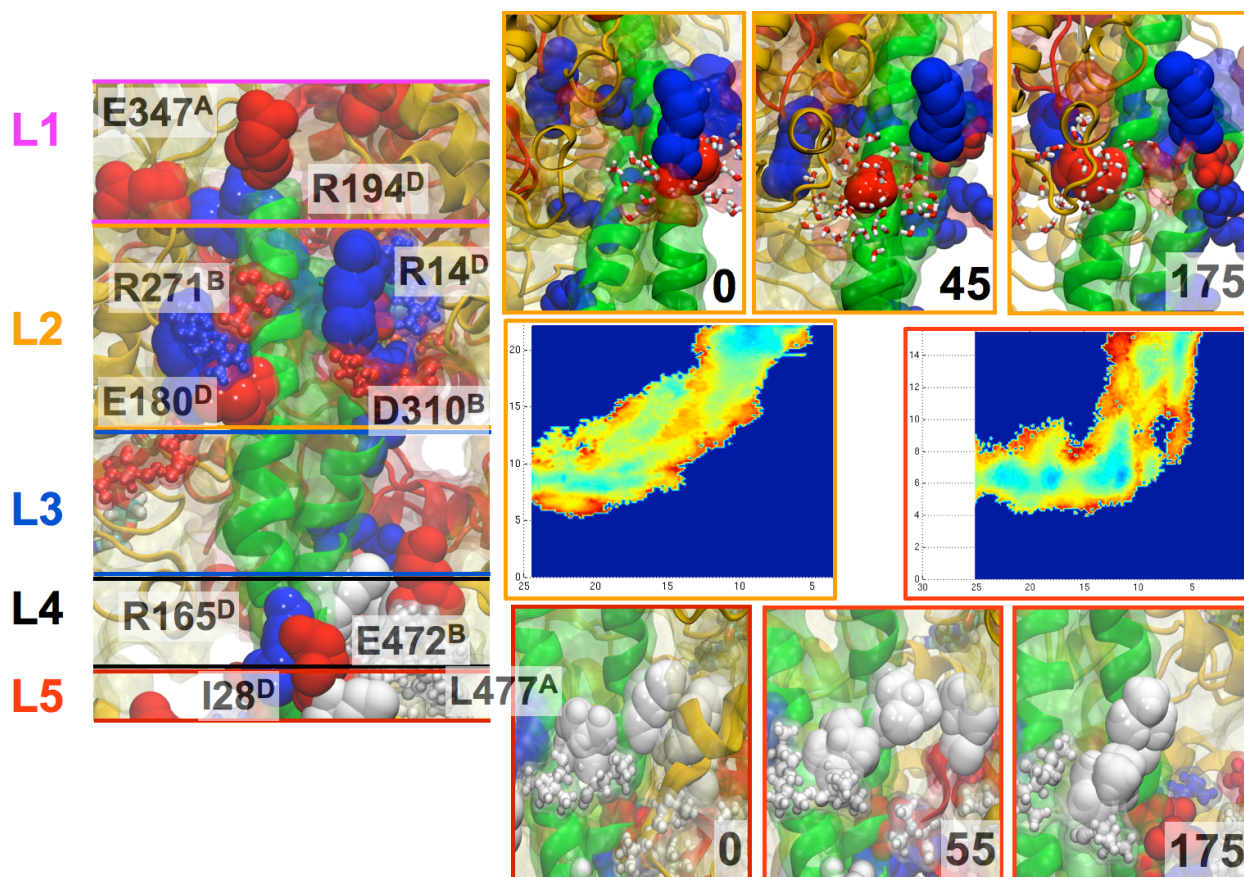


Figure S19: Key pair interactions between the stalk, and A and B domains are illustrated in atomic detail. An electrostatic and a hydrophobic reorganization pathway is displayed, elucidating the role of water in the former and a concerted mechanism for the latter.

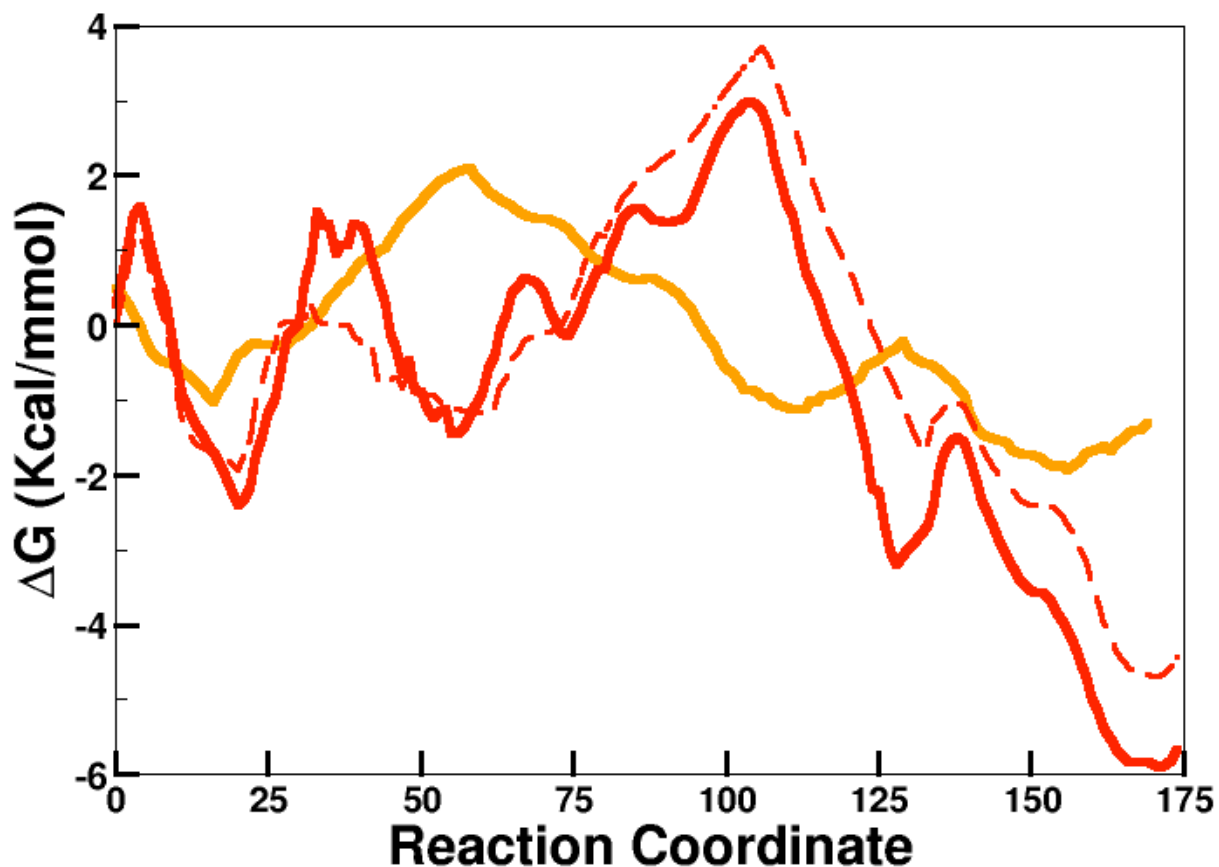


Figure S20: One-dimensional free-energy profiles characterizing the structural transitions of the V_1 -ring (orange), those of the V_1 -rotor (red). While the free-energy profile for the ring is derived out of 1179 collective variables representing the AB interface, that of the rotor further includes positions of the key residues from the stalk (presented in Figures S16 and S19). A third profile (red-dashed) shows the V_1 -rotor free energy changes, but only with the AB interface variables. Close agreement of the free-energy profiles with and without the stalk contribution suggests that majority of the conformational transition energy is harnessed at the AB interfaces. The point of significant energy difference between the two V_1 -rotor profiles is about the state 2 \rightarrow 3 barrier, which is underestimated when the stalk variables are not taken into account.

References

- (1) Schlitter, J.; Engels, M.; Krüger, P. *J. Mol. Graph.* **1994**, *12*, 84–89.
- (2) Pan, A. C.; Sezer, D.; Roux, B. *J. Phys. Chem. B* **2008**, *112*, 3432–3440.
- (3) Jiang, W.; Phillips, J.; Huang, L.; Fajer, M.; Meng, Y.; Gumbart, J. C.; Luo, Y.; Schulten, K.; Roux, B. *Comput. Phys. Comm.* **2014**, *185*, 908–916.
- (4) Landau, L. D. *Statistical physics*; The Clarendon Press: Oxford, 1938.
- (5) Zwanzig, R. W. *J. Chem. Phys.* **1954**, *22*, 1420–1426.
- (6) Zacharias, M.; Straatsma, T. P.; McCammon, J. A. *J. Chem. Phys.* **1994**, *100*, 9025–9031.
- (7) Gumbart, J. C.; Roux, B.; Chipot, C. *J. Chem. Theor. Comput.* **2013**, *9*, 794–802.
- (8) Chipot, C., Pohorille, A., Eds. *Free energy calculations. Theory and applications in chemistry and biology*; Springer Verlag: Berlin, Heidelberg, New York, 2007.
- (9) Johnson, M. E.; Hummer, G. *J. Phys. Chem. B* **2012**, *116*, 8573–8583.
- (10) Hummer, G.; Szabo, A. *Proc. Natl. Acad. Sci. U. S. A.* **2010**, *107*, 21441–21446.
- (11) Park, S.; Khalili-Araghi, F.; Tajkhorshid, E.; Schulten, K. *J. Chem. Phys.* **2003**, *119*, 3559–3566.
- (12) E, W.; Ren, W.; Vanden-Eijnden, E. *Chem. Phys. Lett.* **2005**, *413*, 242–247.
- (13) Maragakis, P.; Spichty, M.; Karplus, M. *Phys. Rev. Lett.* **2006**, *96*, 100602.
- (14) Vanden-Eijnden, E.; Venturoli, M. *J. Chem. Phys.* **2009**, *130*, 194103.
- (15) Chen, M.; Yang, W. *J. Comput. Chem.* **2009**, *30*, 1649–1653.
- (16) Torrie, G. M.; Valleau, J. P. *J. Chem. Phys.* **1977**, *66*, 1402–1408.

- (17) Bartels, C. *Chem. Phys. Lett.* **2000**, *331*, 446–454.
- (18) Shirts, M. R.; Chodera, J. D. *J. Chem. Phys.* **2008**, *129*, 124105.
- (19) Chodera, J. D.; Singhal, N.; Pande, V. S.; Dill, K. A.; Swope, W. C. *J. Chem. Phys.* **2007**, *126*, 155101.
- (20) Gardiner, C. W. *Handbook of stochastic methods: For physics, chemistry and natural sciences*, 2nd ed.; Springer series in synergetics; Springer Verlag, Berlin, Heidelberg, New York, 1985.
- (21) Hummer, G. *New J. Phys.* **2005**, *7*, 34.
- (22) Szabo, A.; Schulten, K.; Schulten, Z. *J. Chem. Phys.* **1980**, *72*, 4350–4357.
- (23) Best, R. B.; Hummer, G. *Phys Chem Chem Phys* **2011**, *13*, 16902–16911.
- (24) Moradi, M.; Tajkhorshid, E. *J. Chem. Theory Comput.* **2014**, *10*, 2866–2880.
- (25) Alam, J.; Arai, S.; Saijo, S.; Suzuki, K.; Mizutani, K.; Ishizuka-Katsura, Y.; Ohsawa, N.; Terada, T.; Shirouzu, M.; Yokoyama, S.; Iwata, S.; Kakinuma, Y.; Yamato, I.; Murata, T. *PLoS One* **2013**, *8*, e74291.
- (26) Alam, J.; Yamato, I.; Arai, S.; Saijo, S.; Mizutani, K.; Ishizuka-Katsura, Y.; Ohsawa, N.; Terada, T.; Shirouzu, M.; Yokoyama, S.; Iwata, S.; Kakinuma, Y.; Murata, T. *Springerplus* **2013**, *2*, 689.
- (27) Kokhan, O.; Wraight, C. A.; Tajkhorshid, E. *Biophys. J.* **2010**, *99*, 2647–2656.